

Real-to-Sim Registration of Deformable Soft Tissue with Position-Based Dynamics for Surgical Robot Autonomy

Fei Liu^{†,1} *Member, IEEE*, Zihan Li^{†,1}, Yunhai Han¹, Jingpei Lu¹, Florian Richter¹ *Student Member, IEEE*
and Michael C. Yip¹ *Senior Member, IEEE*

Abstract—Autonomy in robotic surgery is very challenging in unstructured environments, especially when interacting with deformable soft tissues. The main difficulty is to generate model-based control methods that account for deformation dynamics during tissue manipulation. Previous works in vision-based perception can capture the geometric changes within the scene, however, model-based controllers integrated with dynamic properties, a more accurate and safe approach, has not been studied before. Considering the mechanic coupling between the robot and the environment, it is crucial to develop a registered, simulated dynamical model. In this work, we propose an online, continuous, *real-to-sim* registration method to bridge 3D visual perception with position-based dynamics (PBD) modeling of tissues. The PBD method is employed to simulate soft tissue dynamics as well as rigid tool interactions for model-based control. Meanwhile, a vision-based strategy is used to generate 3D reconstructed point cloud surfaces based on real-world manipulation, so as to register and update the simulation. To verify this real-to-sim approach, tissue experiments have been conducted on the da Vinci Research Kit. Our real-to-sim approach successfully reduces registration error online, which is especially important for safety during autonomous control. Moreover, it achieves higher accuracy in occluded areas than fusion-based reconstruction.

I. INTRODUCTION

Surgical robotic autonomy has drawn significant interest in recent years, as it may help ease surgeon fatigue, reduce human errors, or address lack-of-access to timely, life-saving surgery in remote or under-served communities [1]. Regardless of what type of surgical task is being performed, which is essential for manipulating tissues safely.

Different approaches to 3D reconstruction and tracking from cameras have been proposed for dynamic and deformable environments, such as structure from motion (SFM) [2], simultaneous localization and mapping (SLAM) [3], [4], and fusion-based model-free tracking [5], [6]. A more comprehensive review can be found in [5]. However, visual information alone is not capable of providing internal dynamical properties of soft tissues, such as mechanics, inertial properties – the features that are needed for accurate model-based control.

To address the aforementioned problem, several works have been conducted to estimate the partial tissue dynamics and deformations by using reinforcement learning [7], deformation Jacobian [8], and adaptive estimator [9]. However,

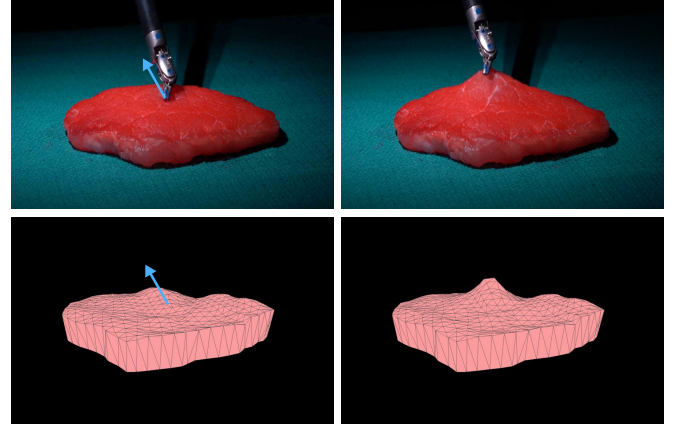


Fig. 1: A demonstration of real-to-sim registration for deformable tissue. The top figures show the real images, and the bottom figures show the corresponding registered meshes before (left) and after (right) manipulation using our method. The blue arrow indicates the grasping direction.

these methods require the complete observation of the deformable tissue and are not able to handle the occlusions. A Finite Element Method (FEM) implemented with the SOFA framework [10] was used in [11] during procedures involving inserting needles into tissues. However, FEM as a general strategy has a significant problem that one cannot explicitly apply position constraints on the simulation easily, so the registration between real world and simulation cannot be well defined. Works in autonomous debridement [12] and tissue tensioning [13], [14] applied learning method to identifying proper tissue properties from visual input. However, none of these works considered the physical dynamics explicitly. They directly extract control policies from vision rather than establish an underlying model and solve the model-based control problem, which limits the performance beyond the training environments.

Another way to integrate tissue dynamics is to build a physical-based surgical simulator. In computer graphics, position-based dynamics (PBD) is a popular method of simulating object deformation [15] in real-time. It has shown great potential in the application for surgical simulation scenarios, such as biopsies [16] and cutting [17].

Taking advantage of fast real-time PBD simulation, we intend to bridge the gap between visual perception and physical tissue dynamics modeling through an online, continuous, real-time registration method. We call this *real-to-sim* registration. The method incorporates the point cloud

[†] Equal contributions.

¹Advanced Robotics and Controls Lab, University of California San Diego, La Jolla, CA 92093 USA. {f4liu, zil027, y8han, jil360, frichter, yip}@ucsd.edu

extracted from cameras at each frame to update the simulated surface particles in PBD. This points-to-particles correspondence can be viewed as a surface constraint and solved as a registration cost function by gradient descent. To the best of our knowledge, this is the first work to perform deformation registration for simulation using PBD, relying on real-world observation of tissue deformation (Fig. 1). The contributions of our method are summarized as,

- 1) a position based framework for surgical simulation involving physical constraints (i.e. distance, volume represented by particles, etc.),
- 2) a real-to-sim matching algorithm for registration is applied as an additional dynamic constraint for PBD,
- 3) integration of surgical perception framework (SuPer) proposed in [5], which can potentially improve the accuracy of fusion-based reconstruction in the occluded areas.

Our method was implemented on a da Vinci Research Kit [18]. Multiple tissue manipulation experiments were conducted to highlight its effectiveness and accuracy. We believe that this *real-to-sim* method is a fundamental step towards generalizable surgical automation.

II. SIMULATION

A. Position-based Dynamics (PBD)

Physical simulation has been studied in the past decades and can be classified into mesh-based ([10], [19]) and mesh-free methods ([20], [21]). For all methods, there is an inherent trade-off between physical accuracy, computational stability, and real-time performance. Unlike physical simulators, the PBD method provides a real-time solver and stable time integration scheme that makes it fast and robust to use in practice. Different materials are identified not by their physical parameters but through constraint equations which define particle positions and position-derivatives. This representation of positional evolution can naturally build the link from visual perception to image data, as it could force a topological constraint on the surface particles of a scene. It also allows us to combine different types of geometrical constraints (such as distance, volume, etc.). More details of PBD method can be found in [15].

In our research, the simulated object is defined as a set of N particles and M constraints. Given the current position \mathbf{x} and velocity \mathbf{v} of the particles, the simulation process is described in Algorithm 1. A force \mathbf{f}_{ext} acts on each particle, which only includes gravity in this work. When a local set of particles is grasped by a manipulator, their positions are constrained to the manipulator's trajectory under the assumption that they are fixed to the end effector.

B. Geometric Constraints

We include several geometric constraints for simulation of the particle dynamics to generate the soft tissue deformation.

1) **Distance Constraint & Volume Preservation:** In [22], the authors proposed a 2D PBD-based surgical simulation framework. In this work, we adapt the same distance

Algorithm 1: Simulation Process

```

1  $\mathbf{x}^* = \mathbf{x}^t + \Delta t \zeta \mathbf{v}^t + \Delta t^2 \mathbf{M}^{-1} \mathbf{f}_{ext}(\mathbf{x}^t)$  ▷ prediction
2 while iter < SolverIterations do
3   for constraint  $C \in \mathcal{C}$  do
4      $[\Delta \mathbf{x}]_C^{iter} = \nabla_{\mathbf{x}^*} C$  ▷ constraint solving
5      $\mathbf{x}^* = \mathbf{x}^* + [\Delta \mathbf{x}]_C^{iter}$ 
6   end
7 end
8  $\mathbf{x}^{t+1} = \mathbf{x}^*$  ▷ update position
9  $\mathbf{v}^{t+1} = (\mathbf{x}^{t+1} - \mathbf{x}^t) / \Delta t$  ▷ update velocity

```

constraint and replace the triangle area preservation with tetrahedron volume preservation.

$$C_{\text{distance}}(\mathbf{x}_1, \mathbf{x}_2) = |\mathbf{x}_1 - \mathbf{x}_2| - d_0$$

$$C_{\text{volume}}(\mathbf{x}_1, \mathbf{x}_2, \mathbf{x}_3, \mathbf{x}_4) = \frac{1}{6} (\mathbf{x}_{2,1} \times \mathbf{x}_{3,1}) \cdot \mathbf{x}_{4,1} - v_0 \quad (1)$$

Where, d_0 is the initial distance between $\mathbf{x}_1 \in \mathbb{R}^3$ and $\mathbf{x}_2 \in \mathbb{R}^3$ and v_0 is the initial tetrahedron volume represented by the four corner particles $\mathbf{x}_1, \mathbf{x}_2, \mathbf{x}_3, \mathbf{x}_4 \in \mathbb{R}^3$. The position corrections $[\Delta \mathbf{x}]_{\text{distance}}$ and $[\Delta \mathbf{x}]_{\text{volume}}$ can be obtained respectively.

2) **Shape Matching:** Shape matching is a geometrically motivated approach of simulating deformable objects [23] to preserve rigidity. The basic idea is to separate the particles into several local cluster regions and then, to find the best transformation that matches the set of particle positions (within the same cluster) before and after deformation, denoted by $\{\hat{\mathbf{x}}_i\}$ and $\{\mathbf{x}_i\}$, respectively.

The corresponding rotation matrix \mathbf{R} and the translational vector $\hat{\mathbf{t}}, \mathbf{t}$ of each cluster are determined by minimizing the total error,

$$\arg \min_{\mathbf{R}^*, \hat{\mathbf{t}}^*, \mathbf{t}^*} = \sum_i^n \|\mathbf{R}(\hat{\mathbf{x}}_i - \hat{\mathbf{t}}) + \mathbf{t} - \mathbf{x}_i\|_2^2 \quad (2)$$

where n represents the number of particles in the corresponding cluster. The detailed solutions can be found in [15] by polar decomposition of the transformation matrix. Thus, the position corrections of shape matching can be computed as

$$[\Delta \mathbf{x}]_{\text{shape matching}} = \mathbf{R}^* (\hat{\mathbf{x}}_i - \hat{\mathbf{t}}^*) + \mathbf{t}^* - \mathbf{x}_i \quad (3)$$

The above constraints can be computed through the Gauss-Seidel method [15] (Lines 3 to 6 in Algorithm 1).

III. REGISTRATION

To ensure our PBD simulator matches the real-world observations, we propose a real-to-sim registration algorithm, which achieves position correction by minimizing a registration cost. The main contribution of our work is bridging the gap between the PBD simulation and a 3D visual observation. In this work we will leverage the perception framework introduced in [5], which is a fusion-based method for surface reconstruction and deformable tissue tracking.

An outline of our real-to-sim registration is shown in Algorithm 2 and visualized in Fig. 2. Signed distance function (SDF) field is used in this work to evaluate the

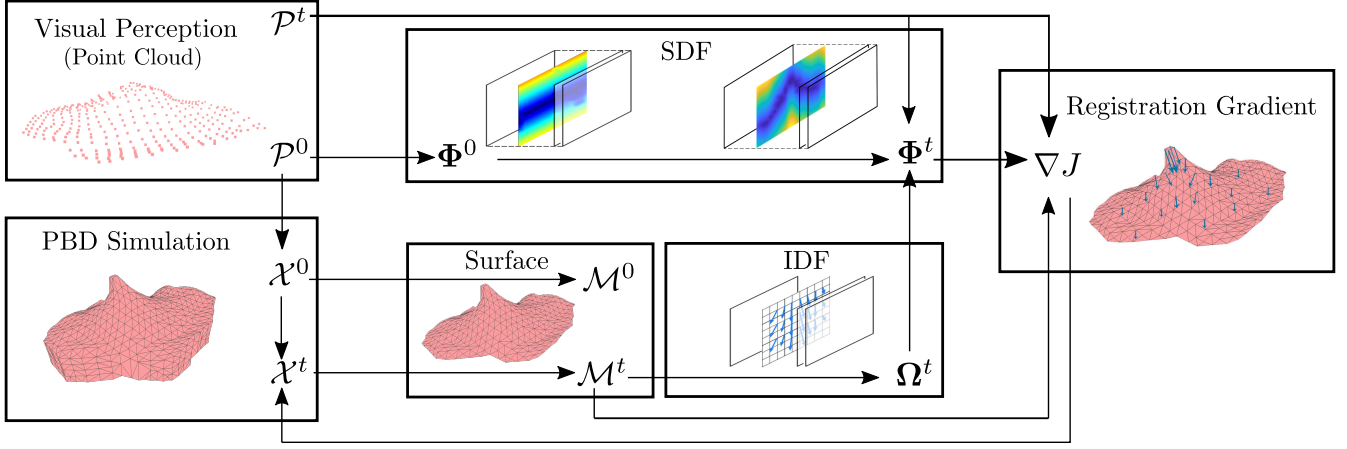


Fig. 2: The real-to-sim registration algorithm flow involves both the observed point cloud and PBD simulation. \mathcal{P}^0 and \mathcal{P}^t are the observed point clouds at time 0 and t respectively. \mathcal{X}^0 and \mathcal{X}^t are the simulated volume meshes (represented by particles) in PBD. \mathcal{M}^0 and \mathcal{M}^t are the extracted surface (a subset of volume mesh) particles. Ω^t is the inverse deformation field (IDF) of \mathcal{M}^0 described along a 3D grid. Φ^0 is the initial signed distance field (SDF) of \mathcal{P}^0 defined along the grid, and Φ^t is the approximated SDF. The registration cost gradient ∇J^t can then be calculated for PBD simulation updates. The math symbols can also be referred to Algorithm 2.

Algorithm 2: Real-to-Sim Registration Flow

input : Initial point cloud \mathcal{P}^0 , registration stiffness λ_{regi}

- 1 $\mathcal{X}^0 \leftarrow \mathcal{P}^0$ ▷ initial PBD particles generation
- 2 $\Phi^0 \leftarrow \mathcal{P}^0$ ▷ initial SDF generation
- 3 $t = 0$
- 4 **while not terminated do**
- 5 $\mathcal{M}^t \leftarrow \mathcal{X}^t$ ▷ extract surface particles from PBD
- 6 $\Omega^t \leftarrow \mathcal{M}^t$ ▷ calculate inverse deformation field
- 7 $\mathcal{P}^t \leftarrow \{\mathbf{p}_1^t, \mathbf{p}_2^t, \dots\}$ ▷ get current point cloud
- 8 $\Phi^t \leftarrow \Phi^0, \Omega^t, \mathcal{P}^t$ ▷ approximate deformed SDF
- 9 $J^t \leftarrow \Phi^t, \mathcal{P}^t$ ▷ calculate registration cost
- 10 $\nabla J^t \leftarrow \mathcal{M}^t$ ▷ calculate registration gradient
- 11 $\mathcal{X}^t \leftarrow \nabla J^t, \lambda_{\text{regi}}$ ▷ perform PBD simulation with registration
- 12 $t \leftarrow t + \Delta t$
- 13 **end**

difference between observed point cloud data and simulated deformation. We firstly define the initial SDF field Φ^0 , in a discrete Eulerian 3D space, using the first frame of reconstructed point cloud data \mathcal{P}^0 (detailed in Section III-A). The SDF indicates the signed distance between a given space point and the initial surface mesh constructed from point cloud \mathcal{M}^0 . Meanwhile, the PBD simulation is also initialized using the initial surface mesh. We extend the surface mesh into a volumetric tetrahedron mesh \mathcal{X}^0 along the gravity direction with pre-assumed thickness of the soft tissue. Then at each time t , we construct an inverse deformation field (IDF) Ω^t by taking the simulated surface mesh \mathcal{M}^t as input (detailed in Section III-B). Thus, the deformed SDF Φ^t of the point cloud \mathcal{P}^t can be approximated by tracing back the surface deformation using IDF Ω^t ,

$$\Phi^t(\mathcal{P}^t) \approx \Phi^0(\mathcal{P}^t + \Omega^t(\mathcal{M}^t)) \quad (4)$$

To sum up, only the SDF field at initial frame Φ^0 is

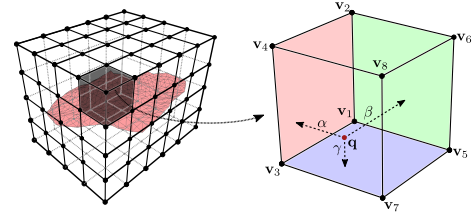


Fig. 3: The boundary space (left) is discretized into Eulerian space grids. The simulated tissue surface is represented by mesh particles inside it. Each space point \mathbf{p} is weighted by its 8 surrounding grid cube vertices \mathbf{v}_i according to the normalized distance to each face.

computed and all other SDF values are estimated by tracing back with the IDF Ω^t . The SDF values are then evaluated as registration cost (detailed in Section III-C) and taken into PBD simulation.

A. Initial SDF Generation

In practice, instead of constructing a continuous 3D SDF field, we only discretize the boundary space that envelops the whole deforming mass into a 3D Eulerian grid \mathbf{V} , as shown in Fig. 3. Only the discrete SDF value at each grid vertex $\mathbf{v} \in \mathbb{R}^3$ is calculated. Then the SDF value of a position within (but not necessarily falling on) this grid can be identified via linear interpolation of its surrounding eight grid cube vertices ($\{\mathbf{v}_1, \mathbf{v}_2, \mathbf{v}_3, \dots, \mathbf{v}_8\}$) in which the point resides. The interpolation weights are calculated according to the normalized distance to each face of the surrounding cube, named by $\{\alpha, \beta, \gamma, 1 - \alpha, 1 - \beta, 1 - \gamma\}$. For any given point in space $\mathbf{q} \in \mathbb{R}^3$, the SDF vector is interpolated as

$$\begin{aligned} \Phi^0(\mathbf{q}) = & (1 - \alpha)(1 - \beta)(1 - \gamma)\Phi^0(\mathbf{v}_1) \\ & + (1 - \alpha)(1 - \beta)\gamma\Phi^0(\mathbf{v}_2) \\ & + (1 - \alpha)\beta(1 - \gamma)\Phi^0(\mathbf{v}_3) + \dots + \alpha\beta\gamma\Phi^0(\mathbf{v}_8) \end{aligned} \quad (5)$$

where $\Phi^0(\mathbf{v}_i), i \in \{1, 2, \dots, 8\}$ is the initial SDF vector for its surrounding grid vertices. This is calculated by the distance to corresponding closest point $\mathbf{p}_*^0 \in \mathbb{R}^3$ inside the

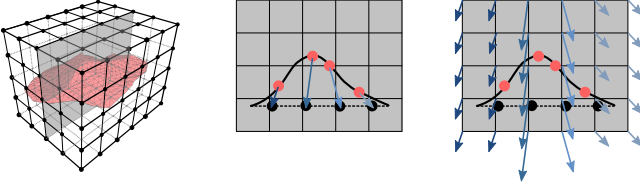


Fig. 4: The demonstration of inverse deformation field (IDF). For simplicity, we visualize the 3D IDF (left) by one 2D Eulerian grid slice (middle and right). Middle figure shows the inverse deformation vectors of current surface particles (red points on solid curve) regarding initial particles (black points on dashed curve). Right figure shows the diffusion of whole grid vertices.

received initial point cloud frame \mathcal{P}^0 . Then, the initial SDF vector for each grid vertex $\mathbf{v} \in \mathbf{V}$ is defined by

$$\begin{aligned} \Phi^0(\mathbf{v}) &= \mathbf{v} - \mathbf{p}_*^0 \\ \mathbf{p}_*^0 &= \arg \min_{\mathbf{p}^0 \in \mathcal{P}^0} \|\mathbf{v} - \mathbf{p}^0\|_2 \end{aligned} \quad (6)$$

B. Inverse Deformation Field (IDF)

An inverse deformation field (IDF) can be computed by tracing back the positions of particles to their initial ones, as shown in Fig. 4. First, for each surface particle $\mathbf{m}_i^t \in \mathbb{R}^3$ in the surface mesh set \mathcal{M}^t at current time t , we can obtain the deformation vector by subtracting the corresponding particle at time $t = 0$, $\mathbf{m}_i^0 \in \mathbb{R}^3$ as,

$$\Omega^t(\mathbf{m}_i^t) = \mathbf{m}_i^0 - \mathbf{m}_i^t \quad (7)$$

where \mathbf{m}_i^t , \mathbf{m}_i^0 can be acquired directly from the PBD simulation.

Then, for all of the discrete Eulerian grid vertices $\mathbf{v} \in \mathbf{V}$ in the initial SDF space, we define their corresponding deformation field vector as,

$$\begin{aligned} \Omega^t(\mathbf{v}) &= \Omega^t(\mathbf{m}_*^t) \\ * &= \arg \min_{\mathbf{m}_*^0 \in \mathcal{M}^0} \|\mathbf{v} - \mathbf{m}_*^0\|_2 \end{aligned} \quad (8)$$

where $*$ is the index of the closest particle to the grid vertex \mathbf{v} in initial surface set \mathcal{M}^0 . It can be viewed as a diffusion operation for each Eulerian grid vertex. For any other point $\mathbf{q} \in \mathbb{R}^3$ in the initial SDF space, the deformation field is calculated using a similar interpolation method as the one shown in Eq. 5.

C. Real-to-Sim Registration Cost

In this section, we define the real-to-sim registration cost function. This registration refers to the matching between the immediate visual perception and the PBD simulation of the current timestamp. The matching cost can be defined as the summation of the deformed SDF values approximated using the surface mesh particles \mathcal{M}^t and all visual perception data, i.e. point cloud \mathcal{P}^t . Suppose $\mathbf{p}_i^t \in \mathbb{R}^3$ is the i -th point in \mathcal{P}^t , then the registration cost function is formulated as

$$J^t(\mathcal{M}^t) = \sum_{i=0}^n \|\Phi^t(\mathbf{p}_i^t)\|_2^2, \quad \mathbf{p}_i^t \in \mathcal{P}^t \quad (9)$$

where n is the number of points in the reconstructed point cloud \mathcal{P}^t .

Since our algorithm consists of multiple discrete grid calculations which precludes analytical gradients, the regis-

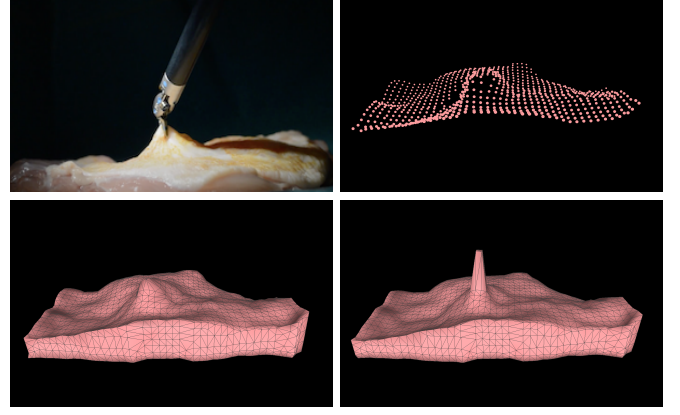


Fig. 5: The demonstration of reconstructed volume meshes on the tissue manipulation dataset. The top-left figure shows the real image and the top-right figure shows the tracked surface particles using the surgical perception framework. The bottom figures show the simulation results, with (left) and without (right) the registration. The estimated mesh is more realistic after the real-to-sim registration.

tration process is performed as a numerical gradient descent via a backwards difference approach,

$$\nabla_{\mathbf{m}^t} J^t = \frac{J^t(\mathbf{m}^t + \Delta \mathbf{m}) - J^t(\mathbf{m}^t)}{\Delta \mathbf{m}} \quad (10)$$

where $\Delta \mathbf{m} \in \mathbb{R}^3$ is a manually assigned small forward deformation of surface particles.

D. Constraint Satisfaction for Real-to-Sim Registration

Traditional point-to-point registration will force all particles on the surface to the observed position, which may violate the object's geometrical structure if the tracking algorithm provides an incorrect correspondence. To avoid this, we perform correspondence-free corrections by minimizing the difference between two surfaces instead of pairs of corresponding points. Since point-to-point correspondences are not strictly enforced, the error can hardly be zero. However, by pulling each simulated particle along the total registration gradient, the points will finally rest in a neighborhood of the observation and consist of a similar tissue surface.

In Eq. 9 and 10, the summation of registration cost J^t and the gradients of each surface particle $\nabla_{\mathbf{m}} J^t$ are obtained, which correspond to another constraint C and $\nabla_{\mathbf{x}} C$ in Algorithm 1, respectively. Thus, the position correction introduced by real-to-sim registration can be directly updated as an additional, soft constraint. We introduce a stiffness parameter $\lambda_{\text{regi}} \in [0, 1]$ to tune this constraint:

$$[\Delta \mathbf{x}]_{\text{registration}} = \lambda_{\text{regi}} \cdot \nabla_{\mathbf{m}} J^t, \quad \mathbf{x} = \mathbf{m} \quad (11)$$

With the stiffness term λ_{regi} , the simulator will not force the surface immediately to the observed point cloud, which avoids oscillation while trying to satisfy different constraints in Gauss-Seidel style.

IV. EXPERIMENTS AND RESULTS

A. Experiment Setups and Evaluation Metrics

In order to demonstrate the effectiveness of the proposed registration framework, we conducted experiments on two

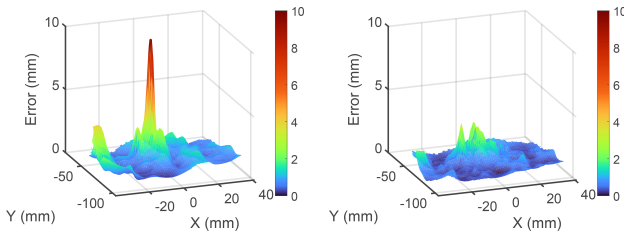


Fig. 6: The visualization of the error between the simulation and observed surface particles before (left) the after (right) the real-to-sim registration (averaged in timestamp). After the registration, the real-to-sim error is reduced significantly around the pinch point.

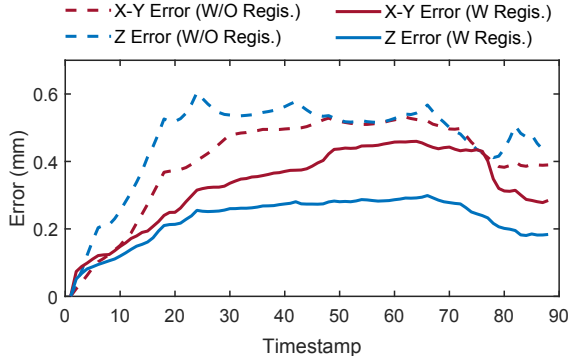


Fig. 7: The real-to-sim registration errors (averaged over all surface particles) on XY -plane and on Z -direction (gravity direction). The errors both in the Z -direction and XY -plane are decreased after registration.

different live environments involving soft tissues manipulated using the da Vinci Research Kit (dVRK [18]): (1) the Chicken Skin Experiment from SuPer dataset [5], and (2) the Pork Steak Experiment, which consists of four motion trajectories: lift, cube, butterfly and sine wave. For each experiment, the visual perception framework [5] was utilized to track the tissue surface point cloud as the real-world observation after masking out the background area. The volume meshes (represented by particles) were created from the initially reconstructed point cloud before the manipulation, and the PBD simulation process started as the control actions were executed.

The control actions involved grasping the surface of the tissue and producing a tissue deformation to track for the real-to-sim method. The grasp location was defined in the simulation by the four closest surface particles to the end-effector. During the registration, their positions were corrected using the shape matching method with the observed point cloud. The simulation boundary conditions were satisfied by fixing the boundary particles' position from the initial volume mesh, where the real chicken skin and pork steak were fixed on the table. This would be representative of an internal cavity where tissue would not typically be separated from connected organ before cutting.

In order to quantitatively evaluate the system performance, we evaluated the registration cost of both whole surface and individual surface particles. We define the evaluation metric as the L_2 norm between the 3D position of the observed point

cloud $\mathbf{p}_i^{obs} \in \mathcal{P}^t$ and the corresponding simulated surface particle $\mathbf{m}_i^{sim} \in \mathcal{M}^t$:

$$\text{Error}_{\text{with/without regis}} = \sum_i^n \|\mathbf{m}_i^{sim} - \mathbf{p}_i^{obs}\|_2 \quad (12)$$

where, n is the total number of simulated surface particles. It is necessary to mention that the evaluation metric defined here is different from the registration cost (which is using SDF) in the previous section, and will be averaged over timestamps or number of particles in the following data analysis. The surface particles are from PBD simulation at each time t . Both the simulation cost with registration and the one without are documented.

B. Chicken Skin Experiment

In this experiment, a surgical tool with a gripper was used to lift the chicken skin, as shown in Fig. 5. If we performed PBD without our registration method, the simulated volume mesh would not deform to the same shape as visually observed. The quantitative comparison results shown in Fig. 6 also support our observation. After performing real-to-sim registration, PBD simulation was able to capture the surface deformation as observed from point cloud. In the left of Fig. 6, the errors around grasping areas is abnormally high due to lack of realistic tissue parameters in simulation, while in the right figure, our method significantly reduce the error between simulation and observation. From Fig. 7, we can tell that our method corrects both the errors in the Z -direction (gravity direction) and in XY -plane. However, the XY errors remain large even after registration. It is caused by the uncertainties, i.e., noises from stereo reconstruction, tracking noises of the surgical tool etc. Meanwhile, the deformation is mostly happening in anti-gravity direction (Z) in our grasping experiments, while only small deformation (in millimeter level) is presented in XY -plane. The noise is relatively large comparing to XY deformation and undermines the real result. Hence, we will focus on the error introduced in the Z -direction in the following experiments.

C. Pork Steak Experiment

In this experiment, we tested our method by manipulating the tissue with four different moving trajectories, which are shown in the first column of Fig. 8. The following columns show the plots of real-to-sim errors in time (averaged over all surface particles) and the heatmaps of the real-to-sim errors in space (averaged over the timestamps) with and without registration, respectively. The experiment results show the importance of online, real-to-sim registration in properly representing the scene deformation.

The areas circled by the black dash lines in the heatmaps are the regions occluded by the surgical tool during the manipulation (see Fig. 9). This information is typically not available, but we were using the SuPer framework [5] for reconstruction, which does spatio-temporal fusion under partial occlusions to estimate their position. Because these points are being only estimated and not measured in the video frame, we can exclude those occluded points from our overall error measurements. The second column in Fig.

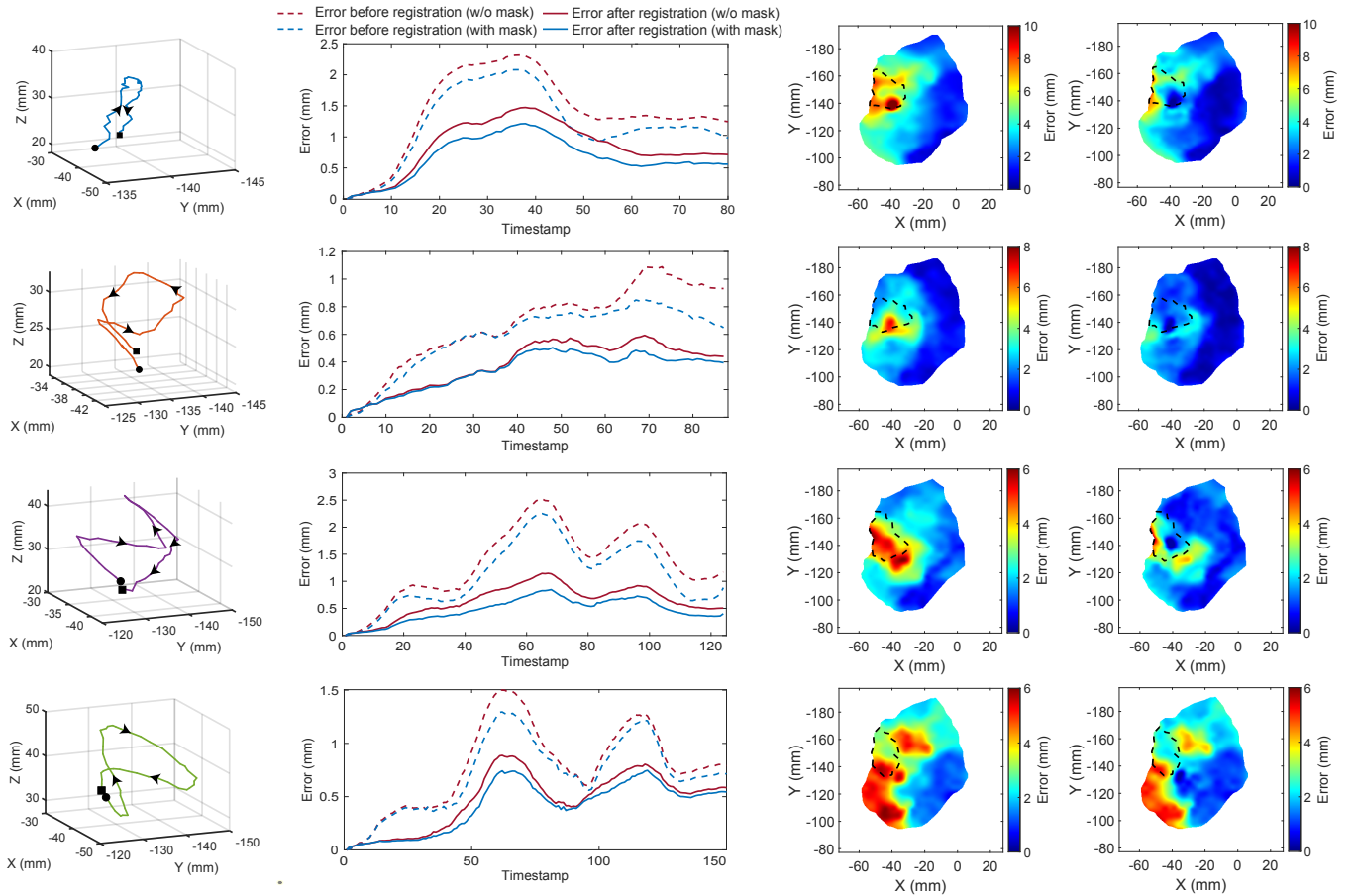


Fig. 8: The quantitative results of the proposed real-to-sim registration method for four different manipulations (one for each row) in Pork Steak Experiment. The plots in the first column show the real tool trajectories (lift, cube, butterfly, and sine wave from top to bottom, respectively). The second column shows the plots of real-to-sim errors before and after registration in time by averaging the surface particles (with and without masking of the occluded particles). The third and fourth columns show the real-to-sim errors in space (averaged over the timestamps) with and without registration respectively. The areas circled by dashed lines indicate the regions occluded by the tool. Our method significantly reduced errors in different manipulation tasks.

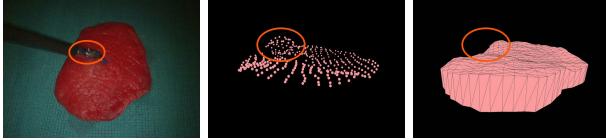


Fig. 9: An example of the inaccurate reconstructions of the regions occluded by the surgical tool. The left figure is the real scene. The middle figure is the observed point cloud and the right figure is the simulation result without registration. The orange circles indicate the occluded regions in each figure. It is obvious that the observation of the occluded regions is inaccurate.

8 shows the mean real-to-sim registration errors (with and without mask) in time. The red solid line shows the error with registration averaging over all surface particles, while the blue solid line shows the averaged error with registration after excluding the particles that are occluded for more than half of the total frames. Since the SuPer framework deals with the occluded area using the history information for fusion, our method provides a more reasonable estimation of the occluded area by using the PBD simulation. This is another contribution of our work.

V. DISCUSSION AND CONCLUSION

In this paper, we have introduced a real-to-sim registration method to initialize and effectively register a PBD simulation to a real, live surgical scene. Several real experiments have been conducted on dVRK with detailed quantitative error analysis. Our method provides a crucial link between volumetric PBD simulations, which is necessary in model-based control, and surface reconstructions of deformable tissue based on camera images.

For future works, we will investigate control policies for surgical automation that use the proposed real-to-sim registration. The proposed geometrical constraints are different from traditional force models using material parameters which may result inaccuracy. More constraints can be exploited to increase realistic of simulation. Furthermore, the registration gradient can be applied to optimizing a control policy for a specific tissue manipulation task using model predictive control.

ACKNOWLEDGEMENT

Many thanks to Hanpeng Jiang for experimental setup.

REFERENCES

- [1] M. C. Yip and N. Das, "Robot autonomy for surgery," *CoRR*, vol. abs/1707.03080, 2017. [Online]. Available: <http://arxiv.org/abs/1707.03080>
- [2] M. N. Cheema, A. Nazir, B. Sheng, P. Li, J. Qin, J. Kim, and D. D. Feng, "Image-aligned dynamic liver reconstruction using intra-operative field of views for minimal invasive surgery," *IEEE Transactions on Biomedical Engineering*, vol. 66, no. 8, pp. 2163–2173, 2019.
- [3] N. Mahmoud, T. Collins, A. Hostettler, L. Soler, C. Doignon, and J. M. M. Montiel, "Live tracking and dense reconstruction for handheld monocular endoscopy," *IEEE Transactions on Medical Imaging*, vol. 38, no. 1, pp. 79–89, 2019.
- [4] J. Song, J. Wang, L. Zhao, S. Huang, and G. Dissanayake, "Mis-slam: Real-time large-scale dense deformable slam system in minimal invasive surgery based on heterogeneous computing," *IEEE Robotics and Automation Letters*, vol. 3, no. 4, pp. 4068–4075, Oct 2018.
- [5] Y. Li, F. Richter, J. Lu, E. K. Funk, R. K. Orosco, J. Zhu, and M. C. Yip, "Super: A surgical perception framework for endoscopic tissue manipulation with surgical robotics," *IEEE Robotics and Automation Letters*, vol. 5, no. 2, pp. 2294–2301, 2020.
- [6] J. Lu, A. Jayakumari, F. Richter, Y. Li, and M. C. Yip, "Super deep: A surgical perception framework for robotic tissue manipulation using deep learning for feature extraction," *arXiv preprint arXiv:2003.03472*, 2020.
- [7] C. Shin, P. W. Ferguson, S. A. Pedram, J. Ma, E. P. Dutton, and J. Rosen, "Autonomous tissue manipulation via surgical robot using learning based model predictive control," in *2019 International Conference on Robotics and Automation (ICRA)*, May 2019, pp. 3875–3881.
- [8] F. Alambeigi, Z. Wang, Y.-h. Liu, R. H. Taylor, and M. Armand, "Toward semi-autonomous cryoablation of kidney tumors via model-independent deformable tissue manipulation technique," *Annals of Biomedical Engineering*, vol. 46, no. 10, pp. 1650–1662, Oct 2018. [Online]. Available: <https://doi.org/10.1007/s10439-018-2074-y>
- [9] F. Zhong, Y. Wang, Z. Wang, and Y. Liu, "Dual-arm robotic needle insertion with active tissue deformation for autonomous suturing," *IEEE Robotics and Automation Letters*, vol. 4, no. 3, pp. 2669–2676, 2019.
- [10] F. Faure, C. Duriez, H. Delingette, J. Allard, B. Gilles, S. Marchesseau, H. Talbot, H. Courtecuisse, G. Bousquet, I. Peterlik, and S. Cotin, "SOFA: A Multi-Model Framework for Interactive Physical Simulation," in *Soft Tissue Biomechanical Modeling for Computer Assisted Surgery*, ser. Studies in Mechanobiology, Tissue Engineering and Biomaterials, Y. Payan, Ed. Springer, June 2012, vol. 11, pp. 283–321. [Online]. Available: <https://hal.inria.fr/hal-00681539>
- [11] Y. Adagolodjo, L. Goffin, M. De Mathelin, and H. Courtecuisse, "Robotic insertion of flexible needle in deformable structures using inverse finite-element simulation," *IEEE Transactions on Robotics*, vol. 35, no. 3, pp. 697–708, 2019.
- [12] S. A. Pedram, P. W. Ferguson, C. Shin, A. Mehta, E. P. Dutton, F. Alambeigi, and J. Rosen, "Toward synergic learning for autonomous manipulation of deformable tissues via surgical robots: An approximate q-learning approach," 2019.
- [13] B. Thananjeyan, A. Garg, S. Krishnan, C. Chen, L. Miller, and K. Goldberg, "Multilateral surgical pattern cutting in 2d orthotropic gauze with deep reinforcement learning policies for tensioning," in *2017 IEEE International Conference on Robotics and Automation (ICRA)*, 2017, pp. 2371–2378.
- [14] T. Nguyen, N. D. Nguyen, F. Bello, and S. Nahavandi, "A new tensioning method using deep reinforcement learning for surgical pattern cutting," *2019 IEEE International Conference on Industrial Technology (ICIT)*, Feb 2019. [Online]. Available: <http://dx.doi.org/10.1109/ICIT.2019.8755235>
- [15] M. Macklin, M. Müller, and J. Bender, "Position-based simulation methods in computer graphics," *Eurographics Tutorial*, 2017.
- [16] E. Tagliabue, D. Dall'Alba, E. Magnabosco, C. Tenga, I. Peterlik, and P. Fiorini, "Position-based modeling of lesion displacement in ultrasound-guided breast biopsy," *International Journal of Computer Assisted Radiology and Surgery*, vol. 14, no. 8, pp. 1329–1339, Aug 2019. [Online]. Available: <https://doi.org/10.1007/s11548-019-01997-z>
- [17] I. Berndt, R. Torchelsen, and A. Maciel, "Efficient surgical cutting with position-based dynamics," *IEEE Computer Graphics and Applications*, vol. 37, no. 3, pp. 24–31, 2017.
- [18] P. Kazanzides, Z. Chen, A. Deguet, G. S. Fischer, R. H. Taylor, and S. P. DiMaio, "An open-source research kit for the da vinci surgical system," in *IEEE Intl. Conf. on Robotics and Auto. (ICRA)*, Hong Kong, China, 2014, pp. 6434–6439.
- [19] W. Tang and T. R. Wan, "Constraint-based soft tissue simulation for virtual surgical training," *IEEE Transactions on Biomedical Engineering*, vol. 61, no. 11, pp. 2698–2706, 2014.
- [20] Y. Duan, W. Huang, H. Chang, W. Chen, J. Zhou, S. K. Teo, Y. Su, C. K. Chui, and S. Chang, "Volume preserved mass-spring model with novel constraints for soft tissue deformation," *IEEE Journal of Biomedical and Health Informatics*, vol. 20, no. 1, pp. 268–280, 2016.
- [21] J. Wang, X. Li, J. Zheng, and D. Sun, "Dynamic path planning for inserting a steerable needle into a soft tissue," *IEEE/ASME Transactions on Mechatronics*, vol. 19, no. 2, pp. 549–558, 2014.
- [22] Y. Han, L. Fei, and M. C. Yip, "A 2d surgical simulation framework for tool-tissue interaction," *arXiv preprint arXiv:2010.13936*, 2020.
- [23] M. Müller, B. Heidelberger, M. Teschner, and M. Gross, "Meshless deformations based on shape matching," *ACM Trans. Graph.*, vol. 24, pp. 471–478, 2005.